The Next Generation of Geomagnetic Field Modelling - utilising low-cost magnetic satellite missions measuring field intensity

Isaac Salt
Richard Holme

1 Abstract

We present an enhanced method of geomagnetic field modelling with total intensity data, using a feature of the dayside field, the equatorial electrojet (EEJ), to estimate the position of the magnetic equator. Combining this with total intensity data may be sufficient to alleviate the effect of non-uniqueness. Our results show a clear benefit to model convergence and reduced residual to the Chaos magnetic field model; however, ultimately the model quality is still compromised, in particular being worse than models constrained by poor-quality vector data. Convergence in model coefficients is improved by a factor of around 10^5 with the EEJ-derived information. Residual to Chaos in the radial component goes from around a maximum of 480nT with intensity data alone, down to a maximum around 300nT with the EEJ. Poor-quality vector data, while yielding a model worse at the poles, still achieve lower residuals around the equator, with a maximum of less than 200nT.

2 Introduction

Over the past 25 years, dedicated satellite missions have provided high-quality vector data on the Earth's magnetic field. This has allowed substantial advances in our understanding of the field. However, with the current multi-satellite Swarm mission coming to an end, there is a need to continue monitoring the field over the next decades.

There is a non-uniqueness in models derived from field intensity data alone, known as the perpendicular error or Backus effect, proved formally by Backus, (1970). A concrete demonstration of this effect leading to large errors was provided using MAGSAT data by Stern et al., (1980). Other methods have been explored involving vector information gathered from ground observatories, which has been shown to reduce the Backus effect. Ultrè-Guèrard et al., (1997) developed this into a method using a model of secular variation to estimate the change in the position of the magnetic equator (where the vertical field is zero) over time; this could then be combined with intensity data to model the field. Unfortunately, ground observatories are unevenly distributed over the planet, with few near the equator, leading to large errors in the secular variation models.

When modelling the field we usually only use with night side data, so as to avoid effects from the Sun. There is, however, a feature of the dayside data which is of interest to us, the equatorial electro-jet (EEJ), a strong electrical current flowing eastward along the magnetic equator in the Earth's ionosphere. The overall effect of the EEJ is a local decrease in total field intensity recorded in the dayside data. This thesis investigates whether we can use the position of the EEJ as a proxy for the magnetic equator, constraining the model by the requirement of a 0 radial component in the magnetic field, at the position of the EEJ.

There is already a proof of concept developed by an earlier student project Holme et al, (2005); this project builds on this to determine in detail whether this method is sufficient to alleviate the Backus effect in practice.

The data are provided by the Chinese CSES Satellite, Xuhui et al. (2018). The satellite has onboard a Search-Coil Magnetometer and a High Precision Magnetometer to measure vector data and total intensity data respectively.

3 The Geomagnetic Field Background

The geomagnetic field can be divided into two parts, arising from sources internal and external to the Earth. The main internal field arises from the motion of conductive material in the core. There are also induced fields in the internal category i.e. the field induced in the crust, and remanent fields resulting from permanent magnetisation of rocks in Earth's crust. External field sources come from currents induced in the magnetosphere and in turn the ionosphere by solar effects.

Ionospheric currents arise due to both the differential heating on the day/night side of the Earth and differential attractions of the Sun and Moon. The resulting fields are designated as solar quiet Sq fields and lunar L fields. These currents cause a daily pattern of variation in the measured horizontal components of the field, i.e., X or Y. The EEJ is part of these Sq effects and causes an abnormally large variation in the horizontal field components near the equator. The overall effect of this in the intensity data is a decrease in total field intensity along the equator. Other, stronger fields are generated at times of high solar activity (so-called magnetic storms); we remove data at such times to avoid errors in modelling.

3.1 Solar Activity and Indicies Kp & Dst

The geomagnetic field is far from static. The main field variation is on a timescale of decades and longer, on the order of 60nT per year. However, the external field exhibits much shorter period variations, due to effects from the solar wind. We characterise these magnetic disturbances in terms of magnetic indices, usually calculated from a combination of measurements from ground observatories. These indices are as described in R. A. Langel (1998).

The K index at each magnetic observatory measures the amplitude range, or difference between the maximum and minimum of a measured horizontal field component after Sq and L effects are removed. Kp is the planetary K index, derived from combined K indices from 13 observatories around the world. Kp is assigned in 3 hour intervals over the day.

When the effects of the solar wind are particularly strong, in what is known as a magnetic storm, the high altitude ring current in the magnetosphere is greatly enhanced. The effect of this includes a large disturbance in the measured horizontal field component near the equator. Dst is a measure of this derived from amplitude range of the measured horizontal field component at low-latitude observatories, this is essentially an equatorial K index. Dst is assigned in 1 hour intervals.

These indices are important to this study since the EEJ is enhanced by magnetic storms; however, if the field is too disturbed the data will be too noisy to reliably determine the position. However, if there is too little solar activity, the EEJ will be weak and may not even show up in the data.

Kp values are retrieved from the GFZ German Research Centre for Geosciences, Postdam and Dst from the World Data Center for Geomagnetism, Kyoto.

3.2 The Crustal Field and Anomalies

There is a field induced by the core field in ferrous material in the crust. This material is found only in trace amounts, but highly variable quantities in rocks in the crust. This causes a complex pattern of what we call anomalies, these can and have been mapped extensively. With many anomalies along the equator, the largest magnitude being the Bangui anomaly, this poses a problem for our EEJ determinations.

The Bangui anomaly, named after the Capital City of Bangui over which it is observed, is a magnetic anomaly that spans the equator. It has a similar signal to the EEJ, although commonly dominates it in the data. This will cause a shift in the measured position of the EEJ away from the equator and must be corrected for.

4 Data Modelling Theory

Data modelling is a process by which we model physical phenomena by using data. We define two stages: forward modelling and inverse modelling. The forward problem is the one we are used to: we start from a physical state and have an *a priori* set of equations to describe the state evolution through space and time. In an effort to model the geomagnetic field we want to start from data and recover the set of equations or 'model' that describes the field. This is known as the inverse problem. The problem is set up in terms of the matrices; $\gamma = y_i$, the data vector or set of all data points, represented as a column vector; $m = x_i$, the model vector or set of all model parameters, again a column vector; and A the forward operator, this is a matrix of linking equations which when right-multiplied by the model vector, gives back the data vector (plus some error). The problem is set up by the equality

$$\gamma = Am + e \tag{1}$$

$$\tag{2}$$

where the quantity $e = \gamma - Am$ is the data residual. We solve this by a least-squares fit, minimising the quantity $e^T e$, the sum of the squared residual. However, in reality there is a covariance between residuals due to either measurement error in the data or effects from parts of the field external to or unaccounted for by our (finite parameter) model. This is represented as a covariance matrix C_e which is determined *a priori* from estimates of error sources. So, the quantity we want to minimise becomes

$$e^T C_e^{-1} e$$

This essentially weights data points by their expected error; if errors are uncorrelated, the only non-zero elements are on the diagonal and the residual is simply divided by the standard deviation. This has the solution

$$m = (A^T C_e^{-1} A)^{-1} (A^T C_e^{-1}) \gamma \tag{3}$$

4.1 Eigenvalue Decomposition of the Inverse Problem

Moving the inverse term to the other side, we write the standard form of the problem as

$$(A^T C_e^{-1} A) m = (A^T C_e^{-1}) \gamma \tag{4}$$

$$\underline{M} m = \underline{r} \tag{5}$$

where the matrix $\underline{M}$ is known as the normal equations matrix and the vector $\underline{r}$ as simply the right hand side (RHS). The eigenvectors of the normal equations matrix form a complete set, meaning we can write the model and RHS as a linear combination of those eigenvectors. Then $\underline{M}$ just multiplies each eigenvector by its eigenvalue and we can solve for the linear expansion coefficients. We can write this as follows

$$\sum_i \beta_i \lambda_i v_i = \sum_i \alpha_i v_i \tag{6}$$

where v_i are the eigenvectors with corresponding eigenvalues λ_i, β_i are the expansion coefficients of the model parameters and α_i are the expansion coefficients of the RHS.

4.2 Instability and Non-uniqueness

Looking at the problem through the lens of eigenvalues is useful because the linear expansion coefficients are related by their eigenvalues as follows

$$\beta_k \lambda_k = \alpha_k \tag{7}$$

$$\beta_k = \frac{\alpha_k}{\lambda_k} \tag{8}$$

where k is the index of a specific eigenvector. The idea of non-uniqueness then follows naturally from imagining $\lambda_k = 0$. It becomes apparent that $\alpha_k = 0$ however, β_k can be anything. In other words, the model coefficient in the direction of the eigenvector k is undefined, and the data contain no information on that model coefficient.

Instability comes from near-zero or small eigenvalues as the α_k coefficient will lead to a large contribution to the model coefficient. This is a problem because of errors in the data, either from random noise or unmodelled sources, remembering α_k is the expansion coefficient of the RHS, we have some error in the RHS vector ϵ and the solution becomes.

$$\beta_k \lambda_k = \alpha_k + \epsilon_k \tag{9}$$

$$\beta_k = \frac{\alpha_k}{\lambda_k} + \frac{\epsilon_k}{\lambda_k} \tag{10}$$

So, the error in the solution (difference between equation 8 and 10) is inversely proportional to λ_k, for small eigenvalues resulting in numerical instability.

4.3 The Geomagnetic Field as an Inverse Problem

When trying to represent a quantity on a sphere it is helpful to think in terms of spherical harmonics. The magnetic potential is the quantity of interest to us, the field is then just $B = -\nabla V$. The potential as represented in spherical harmonics is an infinite sum over degree $0 \to \infty$, the core field dominating degrees up to 14, the crustal field dominant at higher degrees, at satellite altitude contributions above degree 40 are negligable. This series is truncated to a finite maximum degree; for most of our purposes we use degrees up to only 13, this potential takes the form

$$V(\phi, \theta, r, t) = \sum_{n=1}^{13} \sum_{m=0}^{n} g_n^m \cos(m\phi) + h_n^m \sin(m\phi) \left(\frac{a}{r}\right)^{n+1} P_n^m(\cos\theta) \tag{11}$$

The g_n^m and h_n^m are the Lagrange multipliers which represent our model parameters, known as Gauss coefficients. P_n^m is the associated Lagrange polynomial with index n denoting the degree, taken up to $n = 13$ and m denoting the order, taken up to $m = n$ for each degree. There is a dependence on radial distance r, with a as the average radius of the Earth. This term normalises the radial dependence of the potential to the radius of the Earth or in other , notice the potential increases with depth below the surface.

The g_1^0 coefficient has an important physical meaning, this is the coefficient of the axial dipole component of the field. It is also the largest of the coefficients and has the most effect on the position of the magnetic equator, i.e. our measurement.

4.4 The External Field

The field generated from sources external to the core is represented by an additional sum of spherical harmonics term in the potential, with two more Gauss coefficients q_n^m and s_n^m. Note this part of the field is taken only up to degree 1 in our models, meaning 3 coefficients in total, q_1^0, q_1^1, s_1^1. This term has a similar form

$$V_{ext} = \sum_{n=1}^{1} \sum_{m=0}^{n} q_n^m \cos(m\phi) + s_n^m \sin(m\phi) \left(\frac{r}{a}\right)^n P_n^m(\cos\theta) \tag{12}$$

Notice the radial term is inverted; this is what divides the field into internal and external sources. Recall the internal term increases with depth below the surface and decreases above the surface, where the opposite is the case for external sources. The full potential is simply the sum of both internal and external sources.

4.5 Non-Linearity

The magnitude of the field is actually the combination of each component of the field, we have switched here to the NED coordinate system, where (B_x, B_y, B_z) are the North, East, Down components, these are the components of the field in the local plane tangent to the Earth's surface defined by the Z direction. This is the system we use in this study but, the concept is the same for spherical coordinates. The intensity is given as

$$|B| = \sqrt{B_x^2 + B_y^2 + B_z^2}$$

The intensity is now a non-linear function of the Gauss coefficients and we must solve the problem by an iterative least-squares. The data are now a function of the model parameters, rather than a linear transformation.

$$\gamma = f(m) + e \tag{13}$$

$$e = \gamma - f(m) \tag{14}$$

We can linearise the problem about a initial guess using a Taylor expansion. To first order, we write

$$f(m) = f(m_0) + \underline{A}\Delta m \tag{15}$$

where Δm is the change in model parameters $m - m_0$. $\underline{\text{A}}$ is the linearised operator, which differs to our forward operator, containing Fréchet derivatives, describing the rate of change of f with respect to the model parameters. The quantity we want to minimise is then

$$e^T C_e^{-1} e = (\gamma - f(m_0) - A\Delta m)^T C_e^{-1} (\gamma - f(m_0) - A\Delta m) \tag{16}$$

This has a similar solution

$$\Delta m = (A^T C_e^{-1} A)^{-1} (A^T C_e^{-1} (\gamma - f(m_0))) \tag{17}$$

However, this is only an approximate solution and we have to iterate, obtaining a solution when the iteration converges.

5 Method

5.1 Exploring the Data

We have intensity data going back to 2015 but only 2019 for vector data. March 2019 also contains a string of 6 solar quiet, 21-26th which is desirable for modelling. This provides a convenient investigation period for comparing models with vector data, intensity data, and our EEJ method.

The data are provided in files per day, where the spacecraft makes multiple orbits per day - meaning we need to split the files into day/night side if we are to find the EEJ. The Satellite is in sun-synchronous orbit, as outlined in Xuhui et al., (2018), meaning it maintains the same local time for any given point above the Earth's surface. The descending node (point at maximum latitude) is at local time 14:00 and in turn ascending node (point at minimum latitude) at local time 02:00. The data are provided in universal time so we need to convert to local time to do the split into night/dayside.

The time format is a modified Julian date, i.e. decimal days since January 1st 2000. So, if we define the decimal days since the start of each day as d the conversion is

$$LT = d \times 24 + \phi/15 \tag{18}$$

where ϕ is the longitude, the factor of 1/15 is simply the hour time difference per 15 longitude. The local times of the data are all around 2am on the nightside and 2pm on the dayside, 2 and 14 in the data. See Fig 1 for a plot of latitude vs local time, the 26 and -10 values are just because the times are modulo 24, i.e. $26 - 24 = 2$ and $-10 + 24 = 14$ or the remainder of the time divided by 24. Hence 2 and 26 represent the nightside, while 14 and -10 represent the dayside.

We then reconstruct the original data file, just now split into the two groups. Fig 2 is a plot of latitude vs universal time.

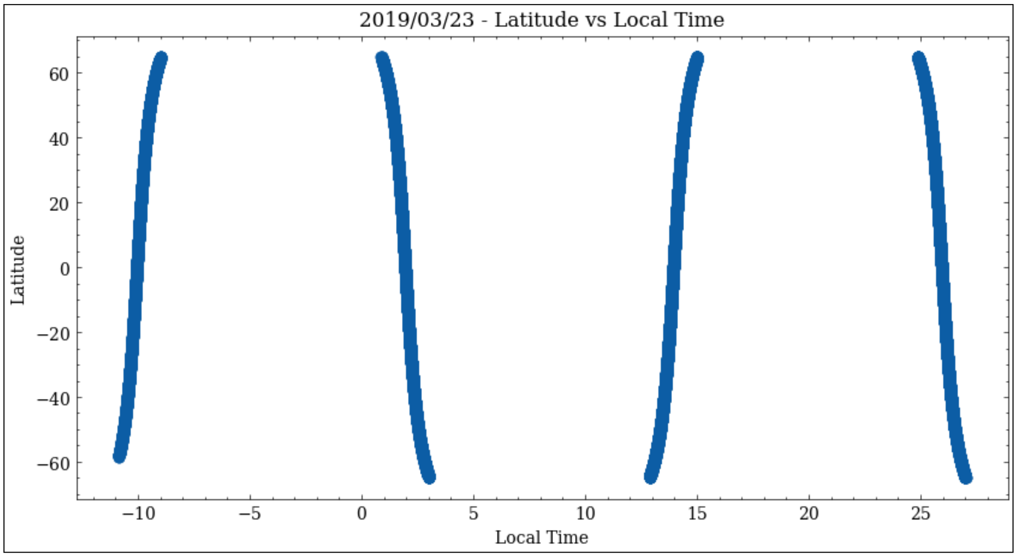

Figure 1: 2019/03/23 - Latitude vs LT, nightside at 2 and 26, dayside at 14 and -10

The spacecraft orbits around 20 times per day, giving us 20 equator/EEJ crossings per day assuming a perfect signal in each crossing. See Fig 3 for an illustration of how the orbit crosses the equator.

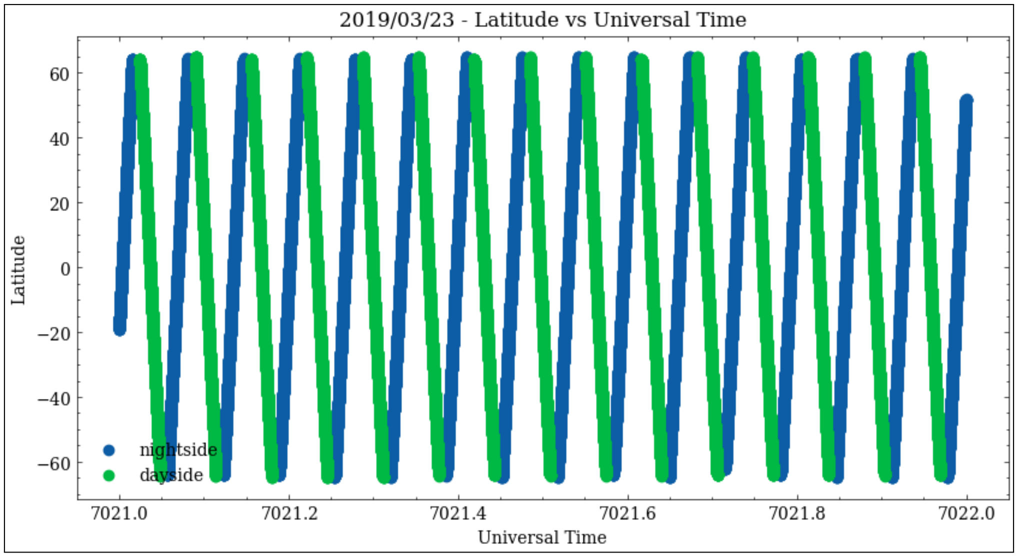

Figure 2: 2019/03/23 - Latitude vs UT, nightside in blue, day side in green

Notice the position of the equator crossings shift from day one to day two, this pattern continues allowing us to obtain EEJ points along the equator.

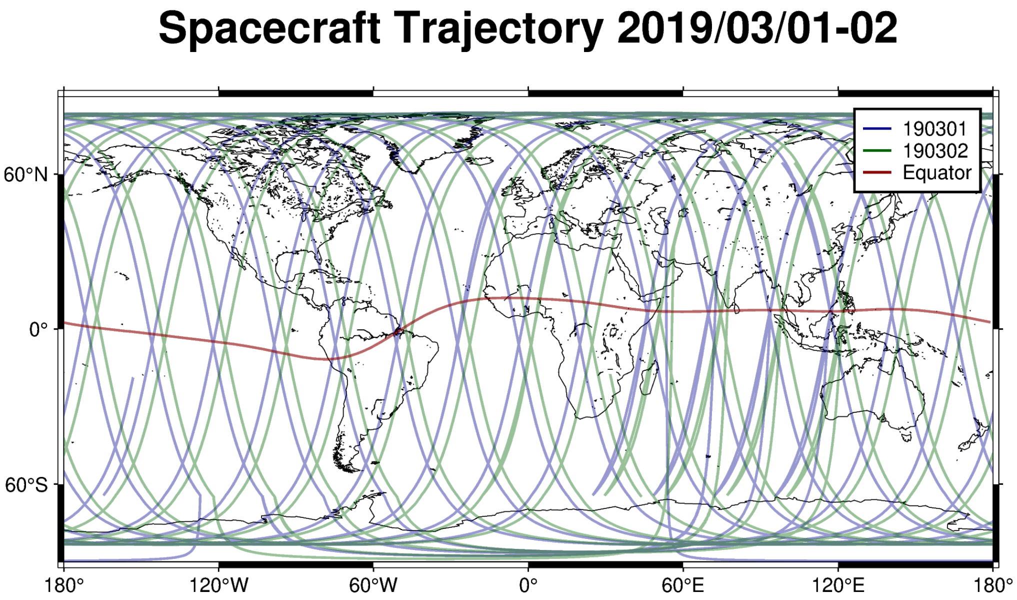

Figure 3: The spacecraft trajectory for two days (blue/green) over the Earth's surface, with the magnetic equator in red. These are full days i.e. both night and dayside

5.2 The Chaos Model

The Chaos model is currently the best representation of the geomagnetic field we have. This model is a time-dependent model for the whole of the satellite era (1999 to present) and for the period of interest constrained by high quality vector data from Swarm. We use the Chaos model as both a starting point and benchmark, meaning we start from this model and, after iteration we compare against the Chaos model. The model is detailed in Finlay et al. (2020).

We can also calculate a magnetic equator from the Chaos model. We call this the perfect equator and use it as an ideal scenario for the EEJ points. We simply take the model predictions for the Z component over a range of latitudes spanning the equator (between around -20 to 20 degrees), and adopt the point closest to zero in the Z component. This is repeated over the entire span of longitudes (-180 to 180 degrees) in one degree steps. This gives us 360 points along the equator, representing the ideal case for the EEJ points. We can then use these points in modelling just as with the EEJ and compare.

5.3 Finding the EEJ

The EEJ signal in the dayside data is an overall decrease in total field intensity. We can measure this by using the predicted intensity of the Chaos model as a"background" signal, and the EEJ will reveal itself in the residual to the dayside data. The spacecraft makes multiple orbits per day so we must further split the data by orbit. This signal appears as a time series with a minimum as the spacecraft crosses over the EEJ, see Fig 4. This minimum can be determined either visually or by fitting a polynomial and taking the data point closest to the calculated minimum. Each is useful in different situations - sometimes the shape is not so clear and it is hard to get a reasonable fit, but visually it still looks reasonable.

However, we would like to be a little more scientific than "Looks reasonable" - Comparing the EEJ against an equator calculated from the Chaos model gives us a much better way of evaluating points. See Fig 9 for a comparison of EEJ points and the equator. This allows us to easily reject orbits/points if they're off the equator, orbits with a clear signal and minimum appear as touching the equator line. So, we take that as the rough benchmark and reject points off the equator.

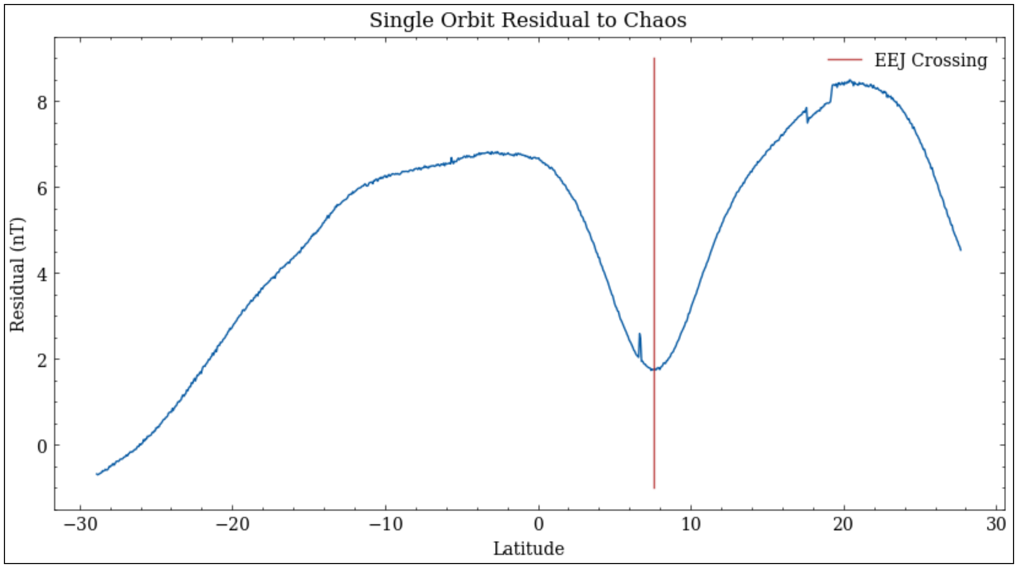

Figure 4: Example EEJ point - taken at the minimum of the polynomial.

We repeat this process for each orbit of each day for the entire month of March 2019.

5.4 External Field Dst Correction

For some days the EEJ is harder to see because of a high Dst index. We can correct for this following the Ørsted Initial Field Model (Olsen et al. 2000). This model provides some extra coefficients

$\tilde{q}_n^m$ and $\tilde{s}_n^m$ which are multiplied by the average Dst throughout the day, and this value is added to each corresponding external coefficient.

Since we are taking an average, this method is only valid when the change in Dst throughout the day is not extreme; however, it turns out it is still possible to get a couple of EEJ points from a particularly variable day. See Fig 5 for a single orbit correction on a somewhat quiet day, average Dst of around 4, with some variation over the day of a maximum of around 6 Dst. Then see Fig 6 for an example of a highly disturbed day with a range over the day of over 25, our Dst correction is no longer valid and while many orbits will be useless, some like this will still have a clear EEJ signal, Kp follows a similar pattern.

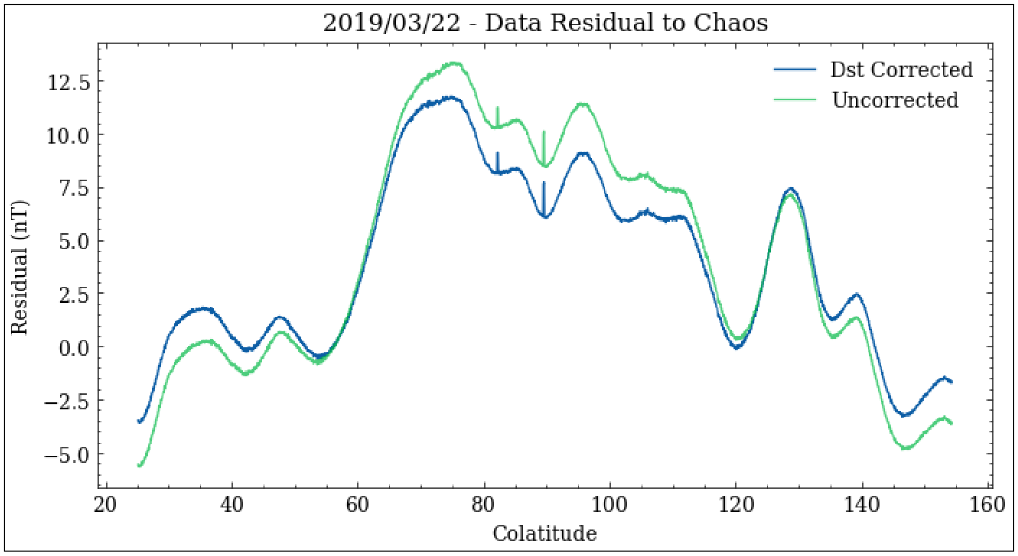

Figure 5: 2019/03/22 Dst correction, average Dst 4, residual of the 2nd orbit

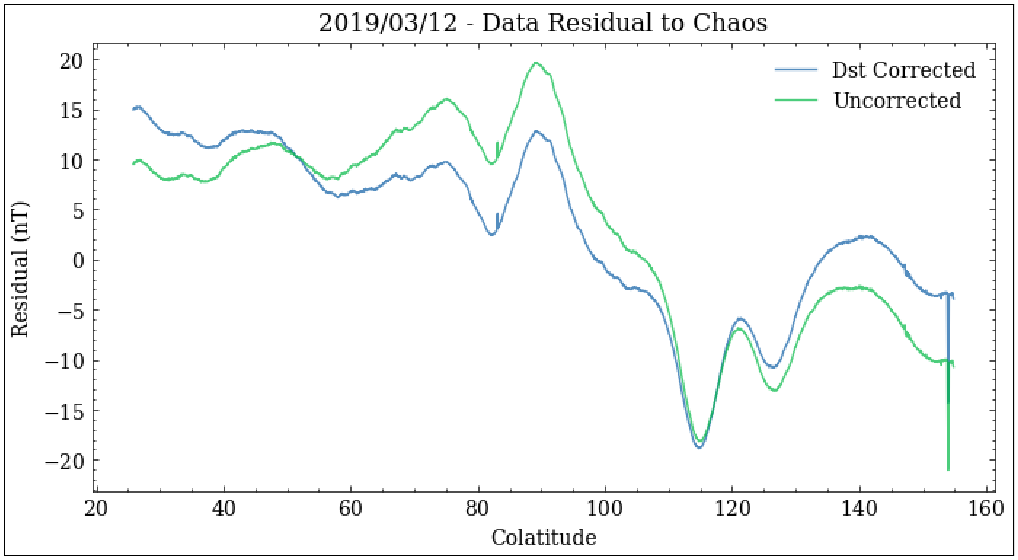

Figure 6: 2019/03/12 Uncorrected residual of the 3rd orbit

5.5 Crustal Field Correction

This part of the field dominates above degree 14 in the spherical harmonic expansion. The Bangui anomaly (longitude 0-20o) is the anomaly that affects us the most in trying to measure the EEJ position, due to its location close to the magnetic equator. The signal is also strong and of similar shape to the EEJ; the combined effect of this in the residual to Chaos is a shift in the polynomial minimum away from the equator.

To correct for this we first need to isolate the signal in the residual. To do this we calculate both the residual with and without the higher degree crust coefficients, denoted core residual and crust residual respectively. Then take the difference between the two residuals - this should reveal any unwanted signal in the core residual. The crustal field is assumed constant over long periods of time, so this correction can be achieved with a reference model. We then subtract this signal from the original core residual, thereby shifting the minimum back towards the equator. See Fig 7 for an example of this process, with the familiar core residual as the green line. The difference in the core and crust residual in red - notice the signal here strongly resembles the EEJ. Finally, the difference between these two lines or crust corrected signal in blue. Visually, its easy to see the shift in the EEJ signal minimum, see Fig 8 for an illustration of how the point moves with respect to the equator.

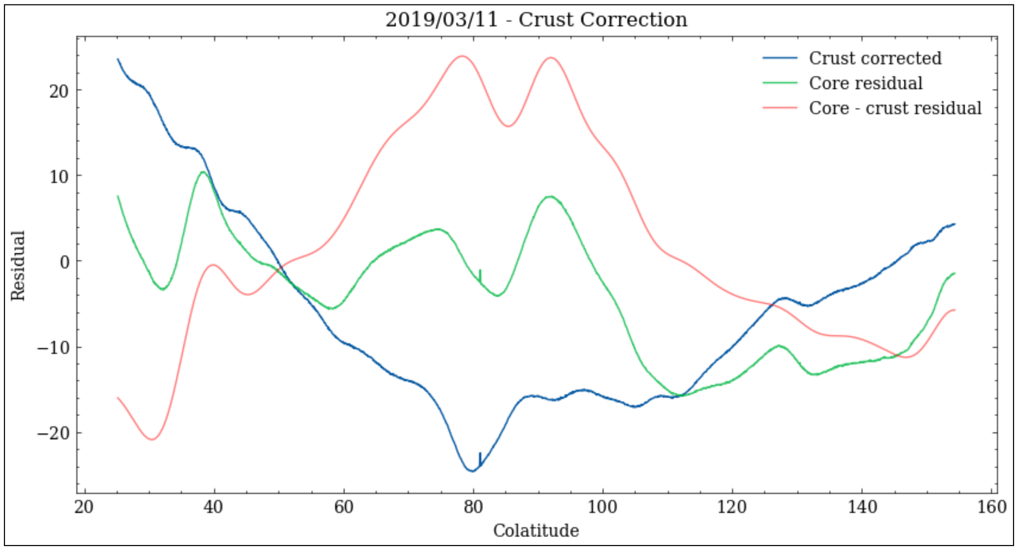

Figure 7: 2019/03/11 - Crust correction example, the corrected residual in blue being the green minus the red line

The crust correction allows us to fill in the gaps present in our first set of EEJ data points, see Fig 9 and 10 for a comparison between before and after correction respectively.

5.6 Vector Data

The modelling with vector data is done in much the same way as intensity data. The data residual of models derived from the vector data were initially very high, due to an issue with the estimated error. A proper treatment requires a model of the satellite attitude error, as outline in Holme (2000); however, for our purposes we simply set the error on each component to be the data residual, 25nT. See 11 for the difference in the measured intensity and the magnitude of the measured vector components i.e. $\sqrt{B_x^2 + B_y^2 + B_z^2}$, the low spread in these two quantities means the lack of

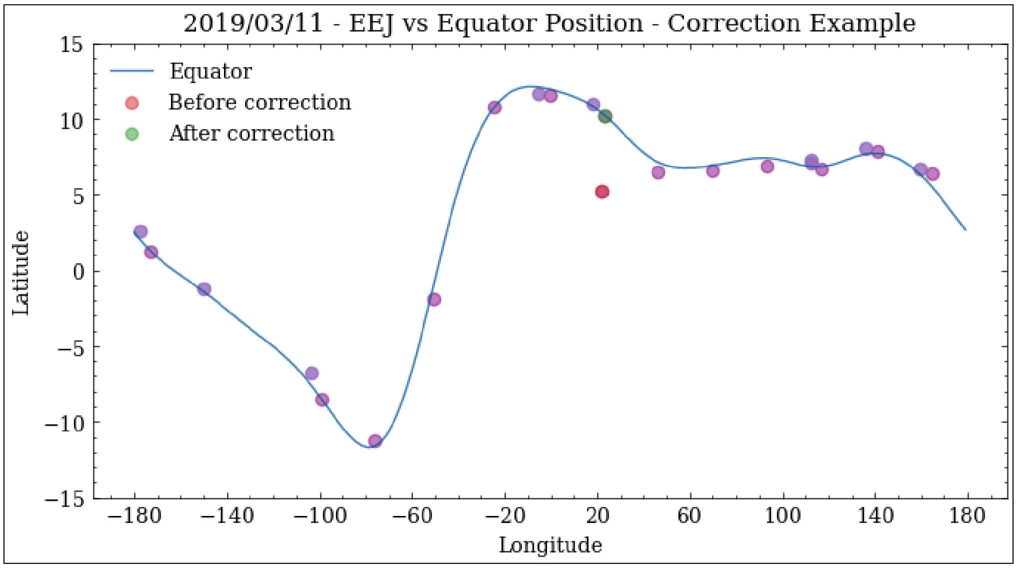

Figure 8: 2019/03/11 - EEJ points vs equator crust correction example (Bangui)

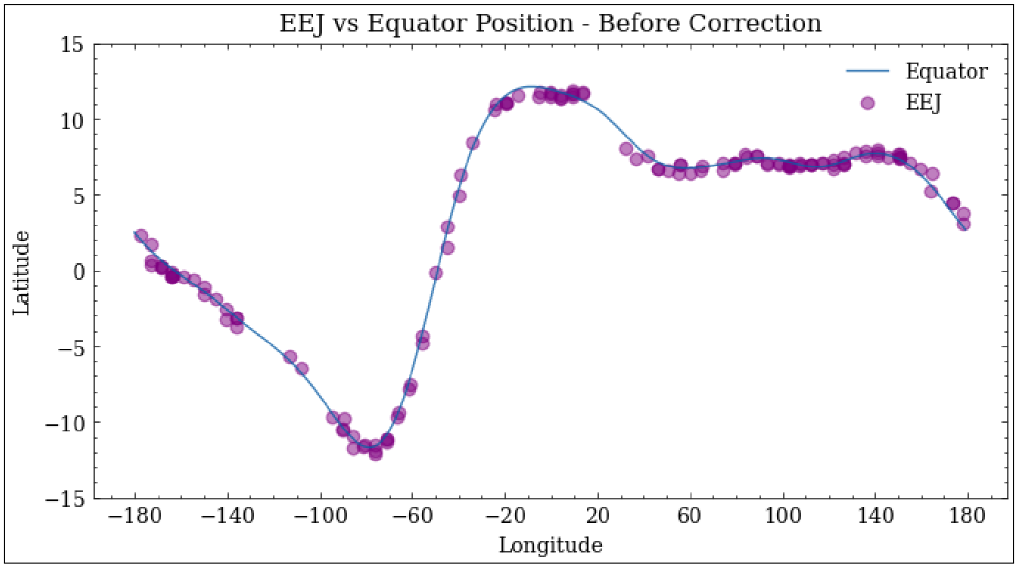

Figure 9: 2019/03 - EEJ points vs equator before crustal correction

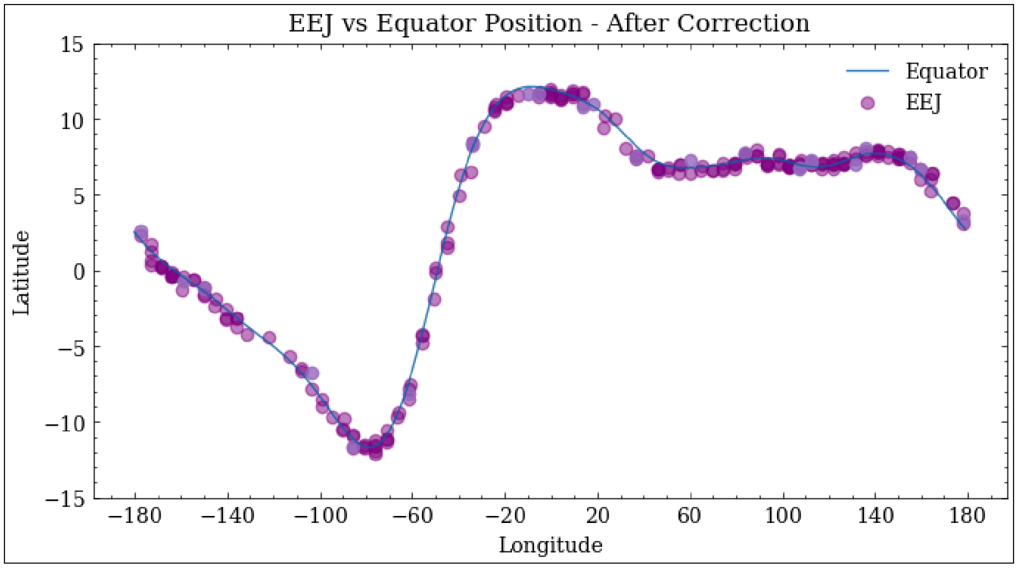

Figure 10: 2019/03 - EEJ points vs equator after crustal correction

proper attitude error treatment won't affect the solution significantly.

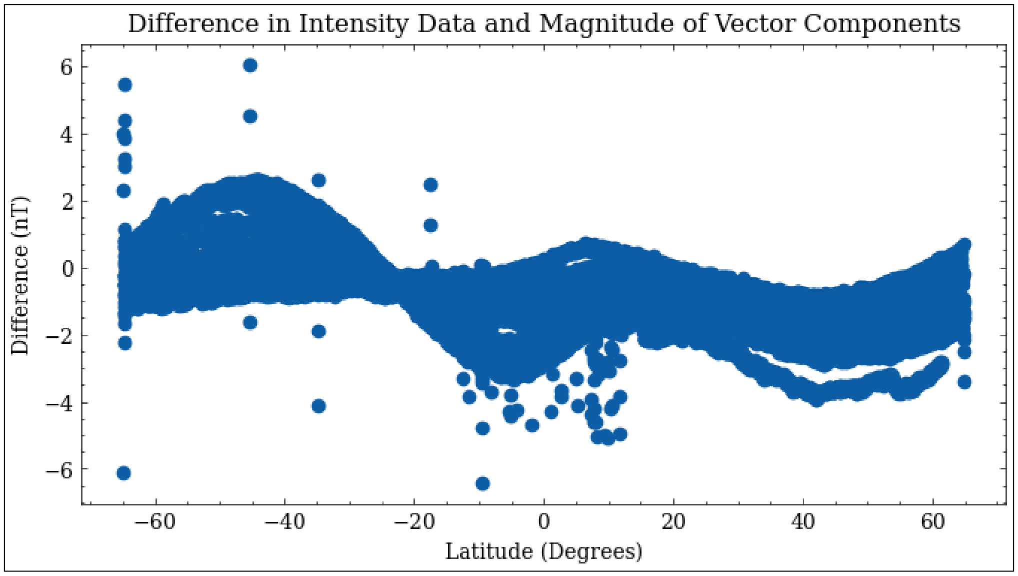

Figure 11: 2019/09/23 Difference in intensity data and magnitude of vector components

We also modify the vector dataset by restricting latitude to within -50 to 50 degrees. This helps alleviate some of the problems at the poles.

6 Results

6.1 Problems With the External Field

When modelling with the external field we noticed large differences to the Chaos model in the axial dipole coefficient and the external field coefficients. This is due to a strong covariance between them.

See Fig 12 for a demonstration of this; notice the large differences in the first and last coefficients. This also causes divergence issues with the solution.

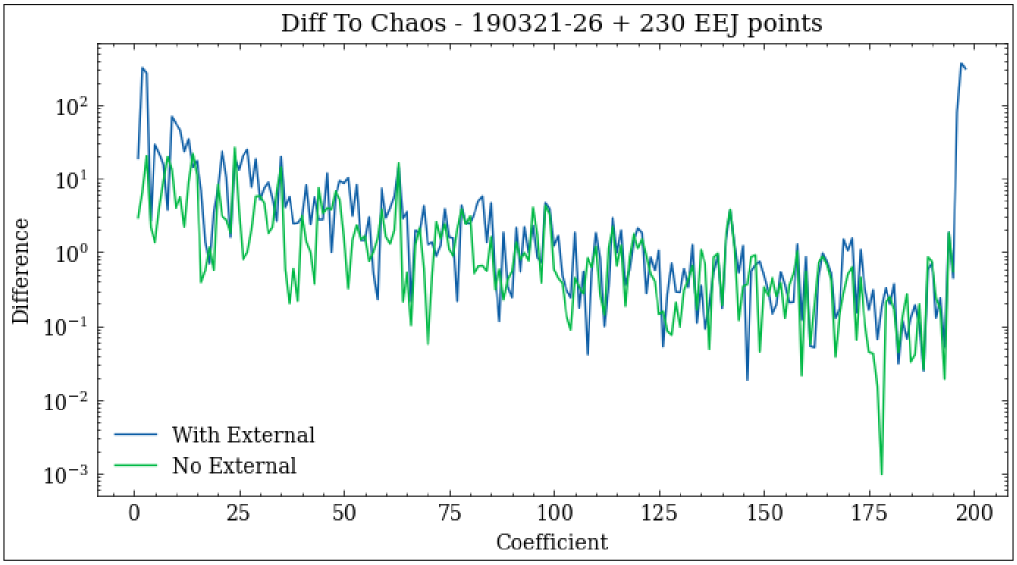

Figure 12: 2019/03/21-26 Difference to the Chaos model in each coefficient

6.2 Convergence

The convergence of a particular solution can be measured by taking the difference between the current and previous iteration, for each coefficient. We do this for every iteration up to 15 and plot the results. We represent the iteration number as an intensity gradient from light at the first iteration to darker colours as iteration number increases.

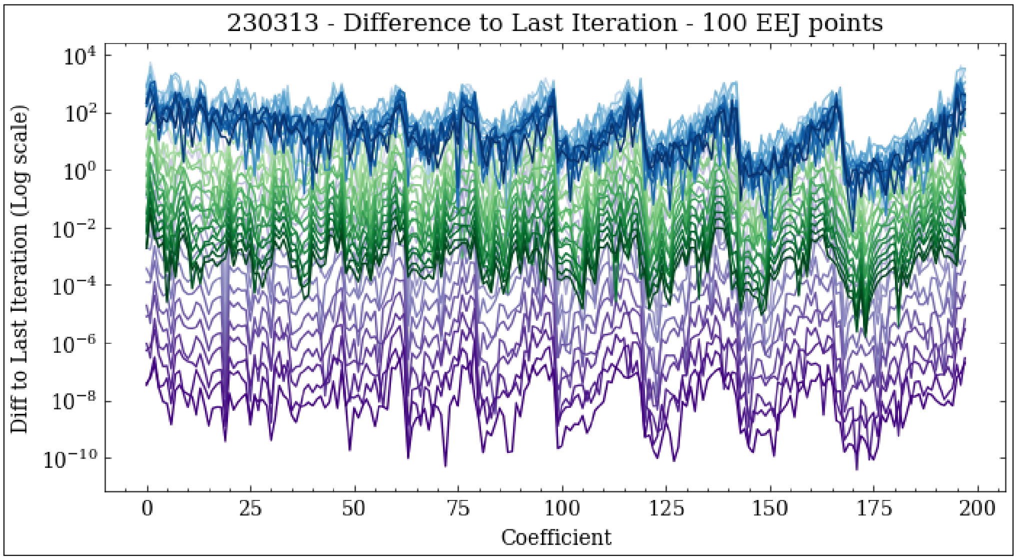

Figure 13: 2023/03/13 - Convergence plot, blue - data alone, green - EEJ, purple - perfect equator

In Fig 13 we show a basic example with a single day of data from March 2023 and just 100 EEJ points. We can see how the solution for the data alone, the blue line, the difference to last iteration

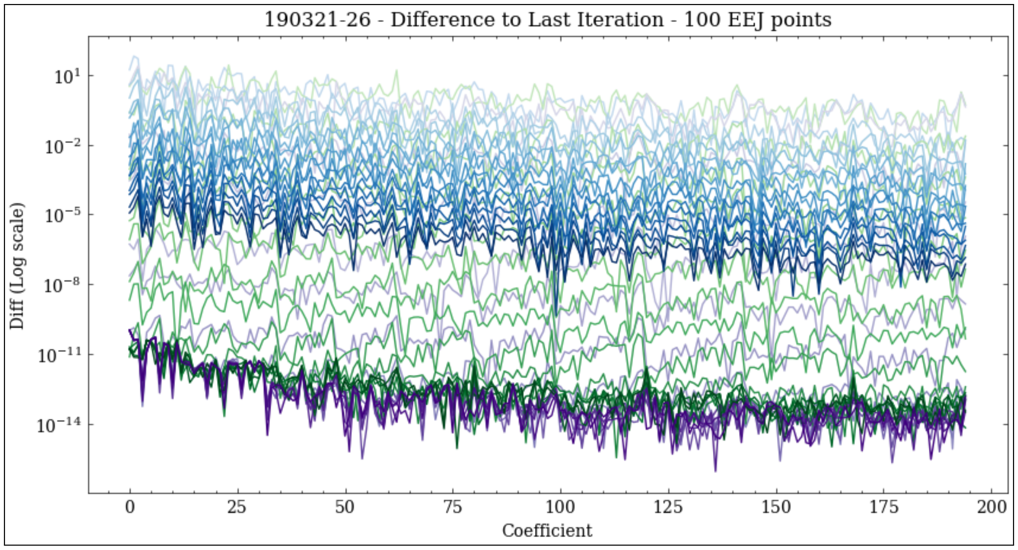

Figure 14: 2019/03/21-26 - Convergence plot, blue - data alone, green - EEJ, purple - perfect equator

sits on the order of around 1-100 - this demonstrates the divergence issues and instability of a solution with intensity data alone. The EEJ line (green) shows the difference to last iteration for a solution with the intensity data combined with 100 EEJ positions; this shows a clear decrease across all coefficients, eventually reaching differences on the order of 0.01-0.001. The purple line is the perfect equator, with 360 points spanning the entire longitude range in 1 degree steps. This represents the ideal scenario, if the EEJ points were exactly on the equator, here we see a similar effect again but just to a greater magnitude. Here we also see the problems with the external field, with there being a large difference in the degree 1 and external coefficients.

In Fig 14 we show the 6 quiet days of particular interest to us as discussed earlier. In this plot we can see the data alone is better on its own due to the extra days of data. The EEJ line, with 100 points is still a clear improvement with this line being closer to the perfect equator than in Fig 13. Bear in mind we are no longer modelling the external field in this plot, hence the improved convergence in the degree 1 coefficient. The effect of more EEJ points has little effect above 100 on convergence beyond this, as expected if it's already converging to 14 decimal places.

6.3 Mapping the Chaos Residual

We evaluate our models by comparisons to the Chaos model. We do this by taking the difference in each coefficient between our model and the Chaos model, Chaos residual will now refer to this difference (not the data residual to Chaos). We can then produce maps of the Z component over the Earth, measuring the difference in model predictions. See Figure Fig 15, 16, 17 for the three main of most interest - Intensity data alone, data + 230 EEJ points, and data + Eq respectively.

See Fig 19, 20, 18 for the comparison to vector data - Same EEJ and Eq model but at 200nT scale and the vector model.

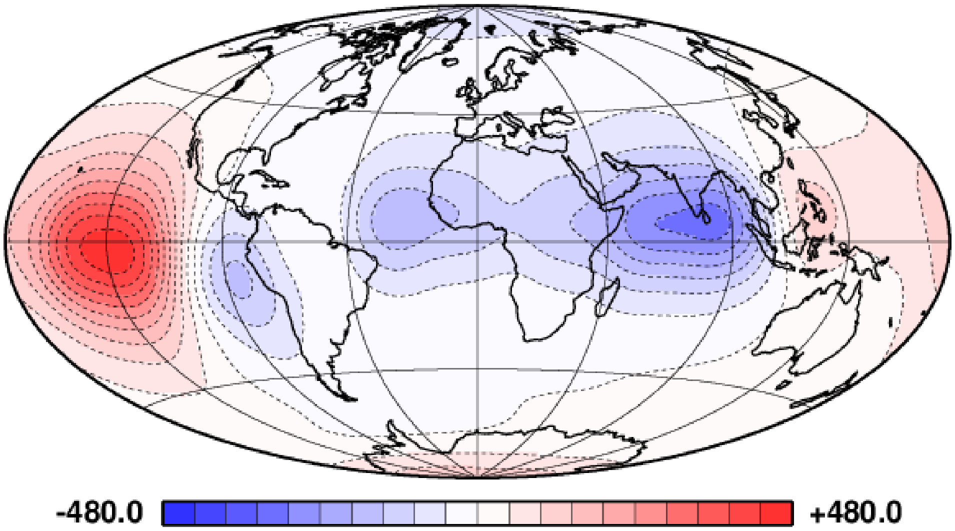

Figure 15: 2019/03/21-26 Chaos Residual Map - Intensity data alone, 480 nT scale, data residual - 1.27

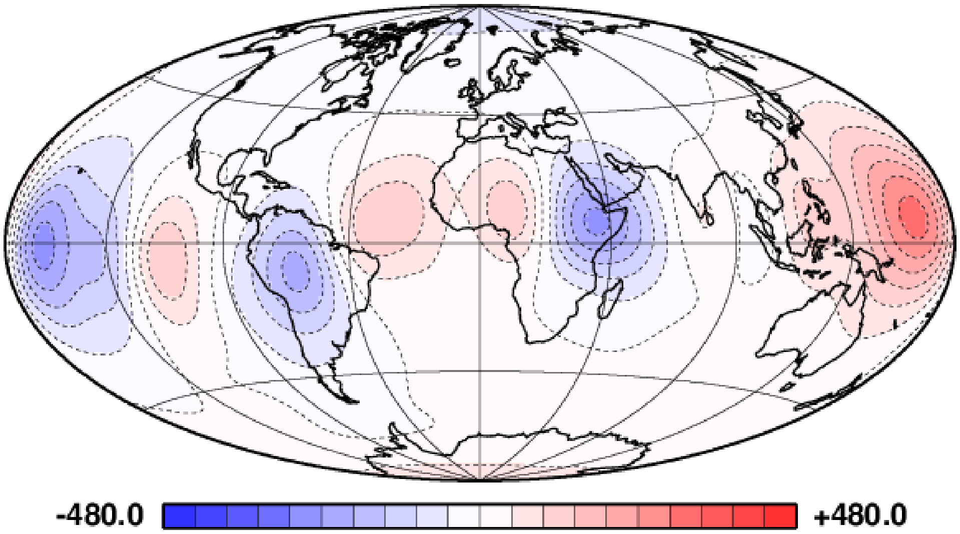

Figure 16: 2019/03/21-26 Chaos Residual Map - Intensity data + 230eej points, 480nT scale, data residual - 1.97

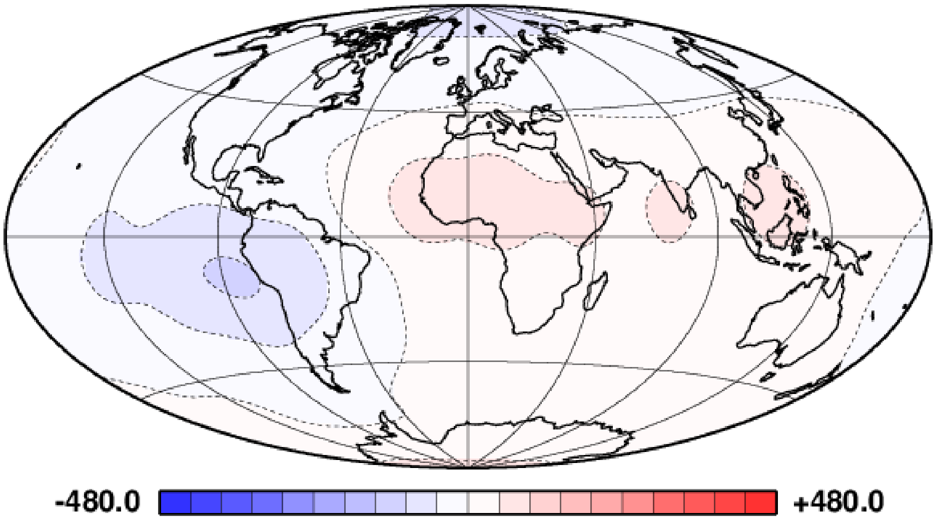

Figure 17: 2019/03/21-26 Chaos Residual Map - Intensity data + perfect equator, 480nT scale, data residual - 1.29

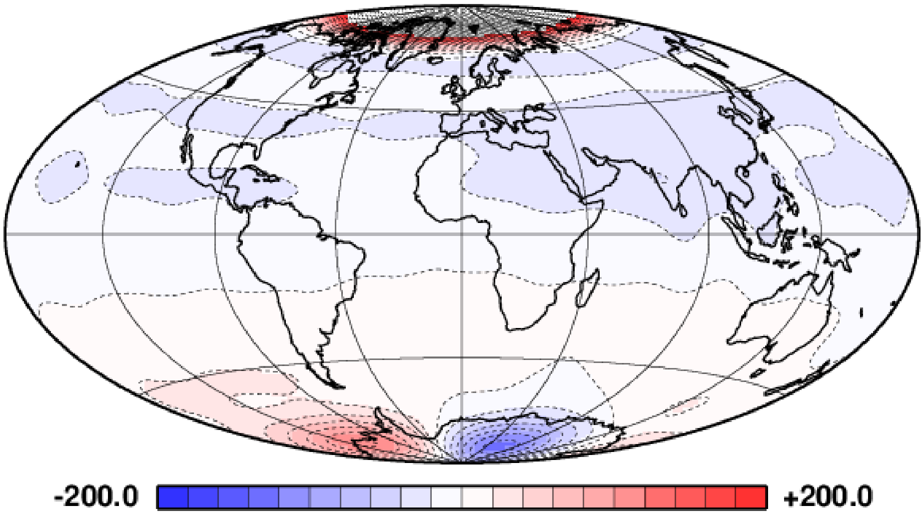

Figure 18: 2019/03/21-26 Chaos Residual Map - Vector data, 200nT scale

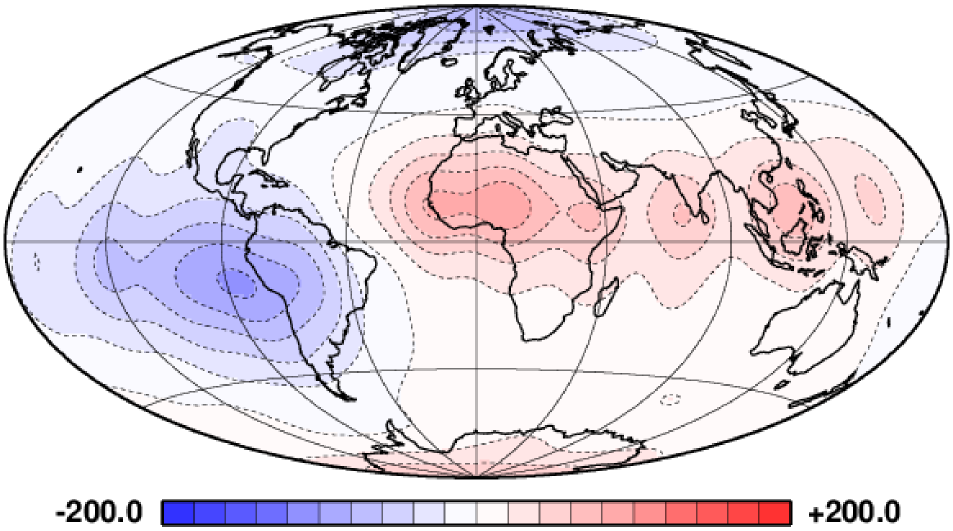

Figure 19: 2019/03/21-26 Chaos Residual Map - Intensity data + perfect equator, 200nT scale

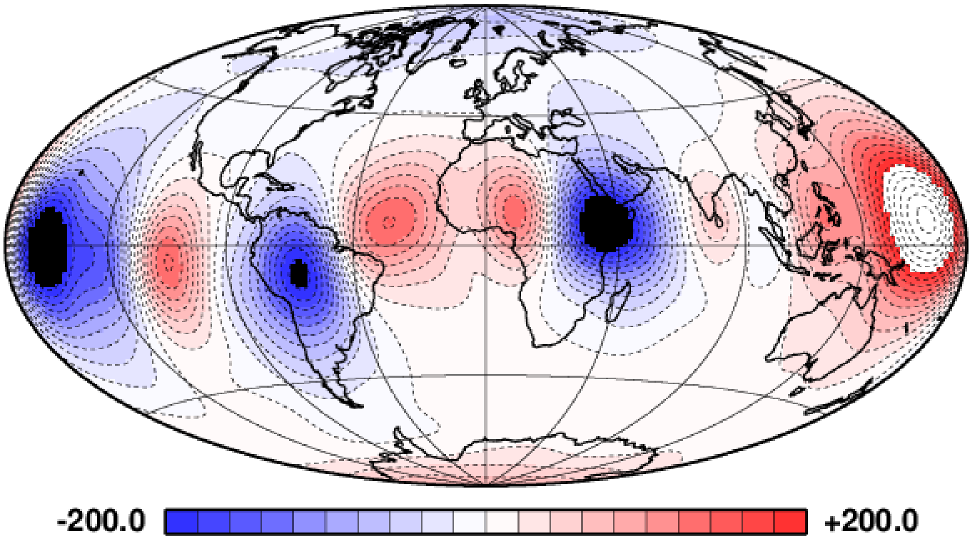

Figure 20: 2019/03/21-26 Chaos Residual Map - Intensity data + 230 EEJ points, 200nT scale

6.4 The Data Residuals

We can also look at the data residuals from our models. See Fig 21 for the residuals in the Z component for our 230EEJ model and the Chaos model. This shows the error in our EEJ positions. See Fig 22 for the difference between these two. The periodic shape of this plot is interesting, it represents the difference in the determinations of the magnetic equator for each model. Notice how this lines up with the maps for the 230EEJ model, since this is essentially measuring the same thing.

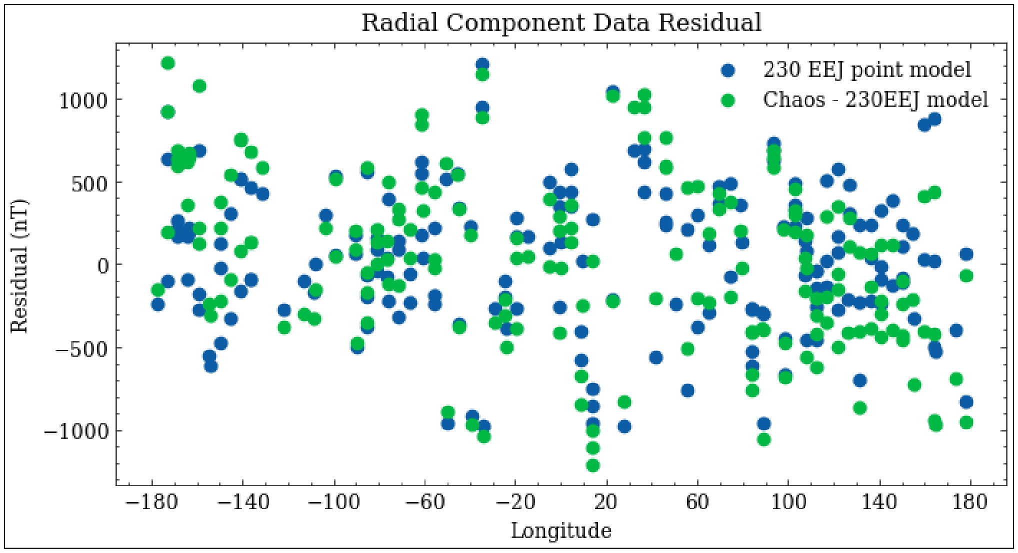

Figure 21: 2019/03/21-26 - The residual in the Z component of the EEJ positions for 230EEJ and Chaos model

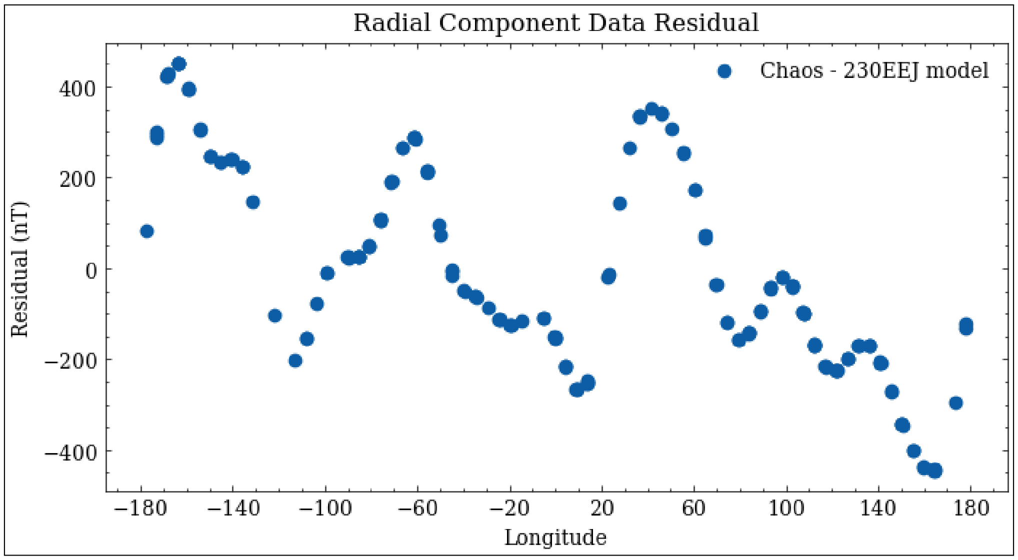

Figure 22: 2019/03/21-26 - The difference in the Z component residual for 230EEJ model and Chaos

6.5 Power Spectra

Another way to look at the field is the mean-squared field of power of the model difference. See 23 for a demonstration of the difference in the power spectra between our 230 model and Chaos, and 24 for the vector model.

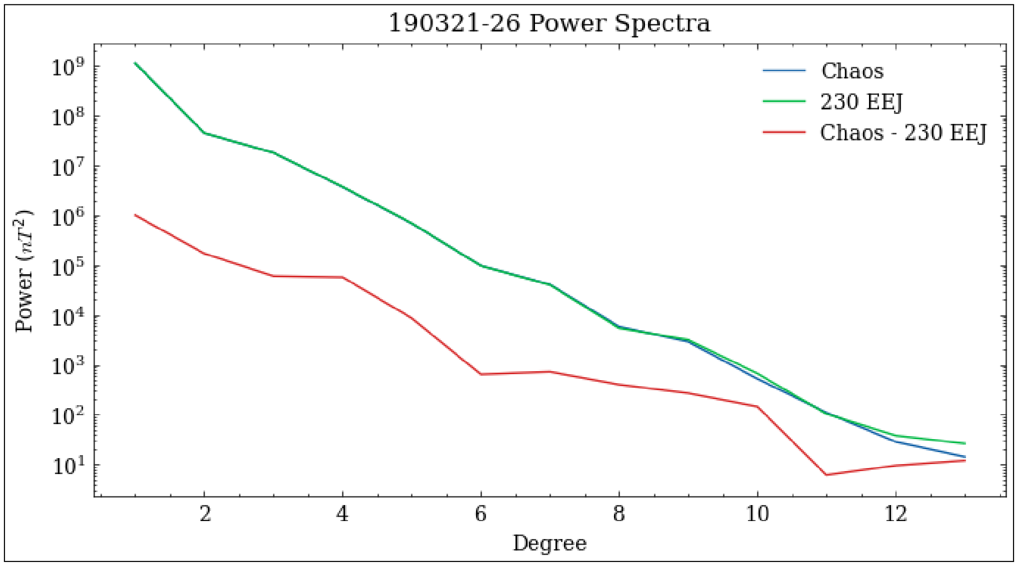

Figure 23: 2019/03/21-26 Comparison of power spectra obtained from the Chaos model and our 230 EEJ model

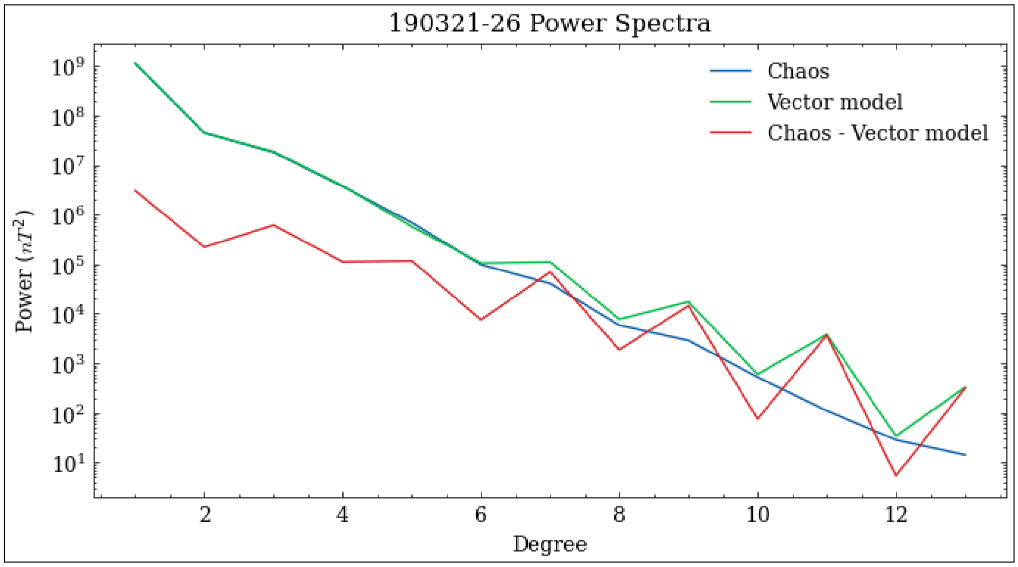

Figure 24: 2019/03/21-26 Comparison of power spectra obtained from the Chaos model and the vector model

6.6 The Eigensolution

We can also look at our solution through the eigenvalue eigenvector lens. See Fig 25 for a comparison of the eigenvalue spectra for the data, EEJ and Eq models. The benefit here is very clear in raising the eigenvalue of those low eigenvalue eigenvectors. A 230 EEJ model with the external field coefficients included is also shown – notice the sharp drop-off in eigenvalue magnitude at the external coefficients (last 3 coefficients, after other lines end)

Looking to the eigenvectors, for a degree 13 model we have 195 vectors with 195 components each. To visualise these we can look at the component of the Chaos model along the eigenvectors, in other words we project the true field onto the eigenvalues of our 230EEJ solution. See Fig 26, this plot has some very specific peaks in higher index eigenvectors. This is alarming as the eigenvectors are loosely in the order of descending eigenvalue. See Fig 27 for a plot of the components of each eigenvector. Following see Fig 28 and 29 for the familiar Z component maps but this time showing the field from each eigenvector.

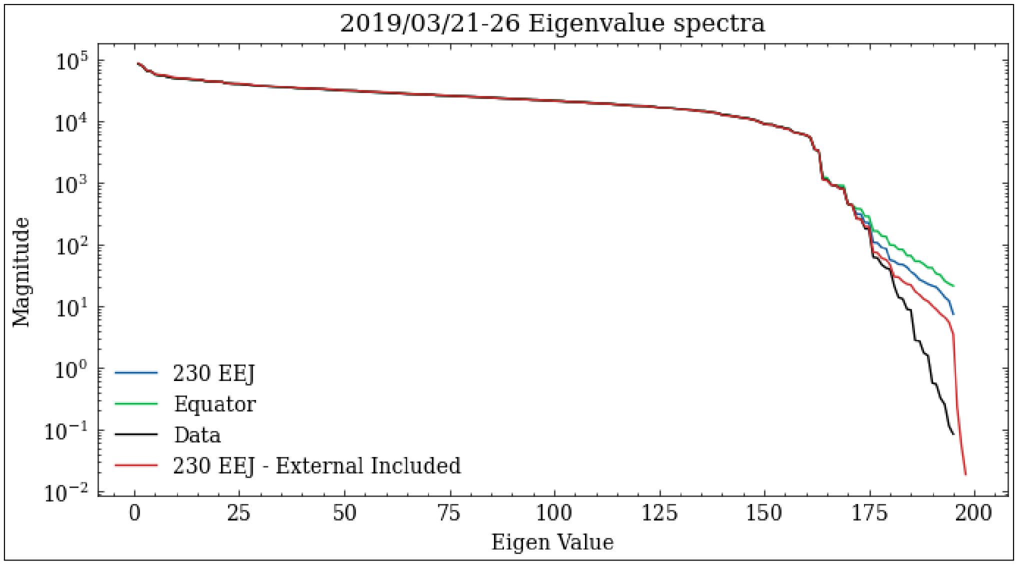

Figure 25: 2019/03/21-26 Eigenvalue Spectra - Comparison between EEJ, Eq, and data alone

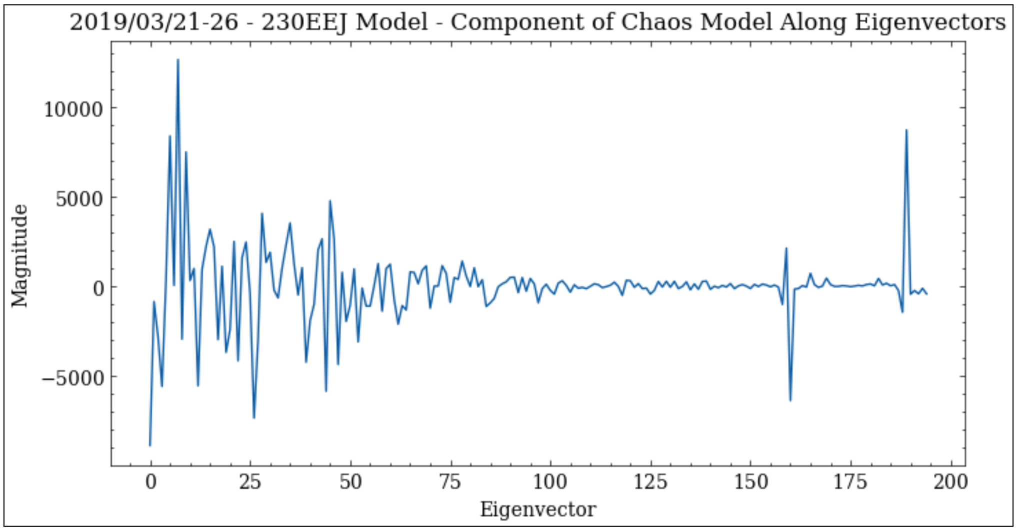

Figure 26: 2019/03/21-26 Eigenvalue Spectra - The component of the Chaos model along the eigenvectors of the 230 EEJ model

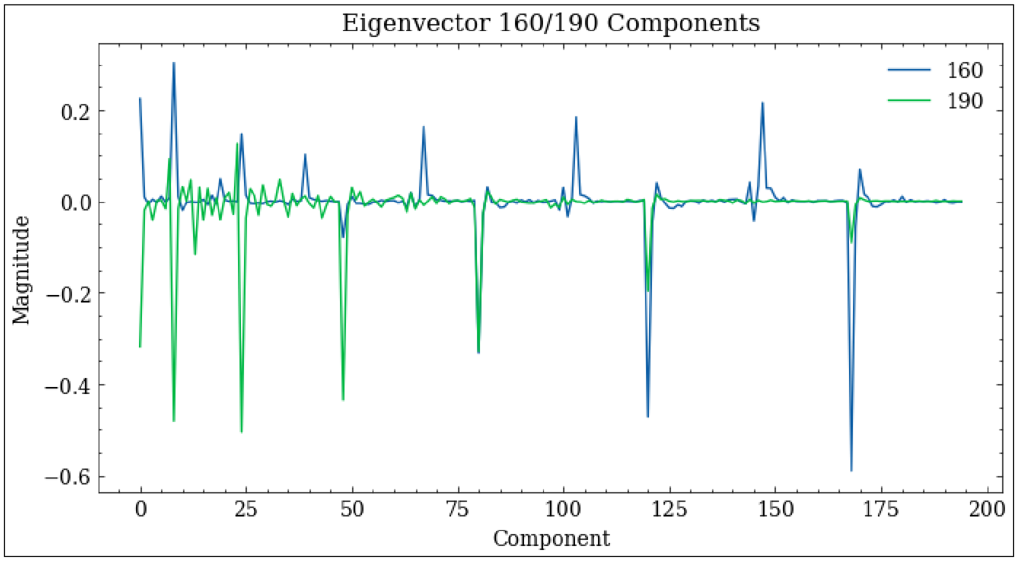

Figure 27: 2019/03/21-26 230 EEJ model - Eigenvectors 160 and 190

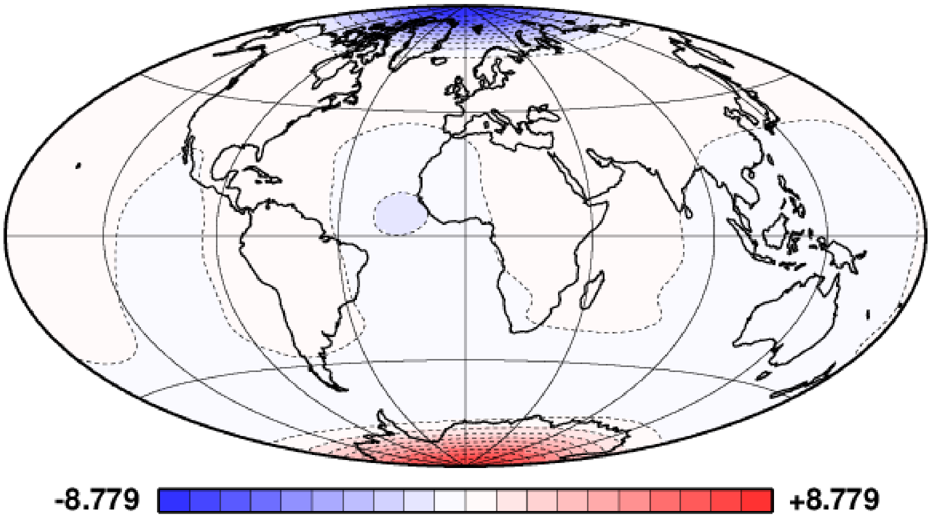

Figure 28: 2019/03/21-26 230 EEJ - Z component map, eigenvector 160, eigenvalue 6000

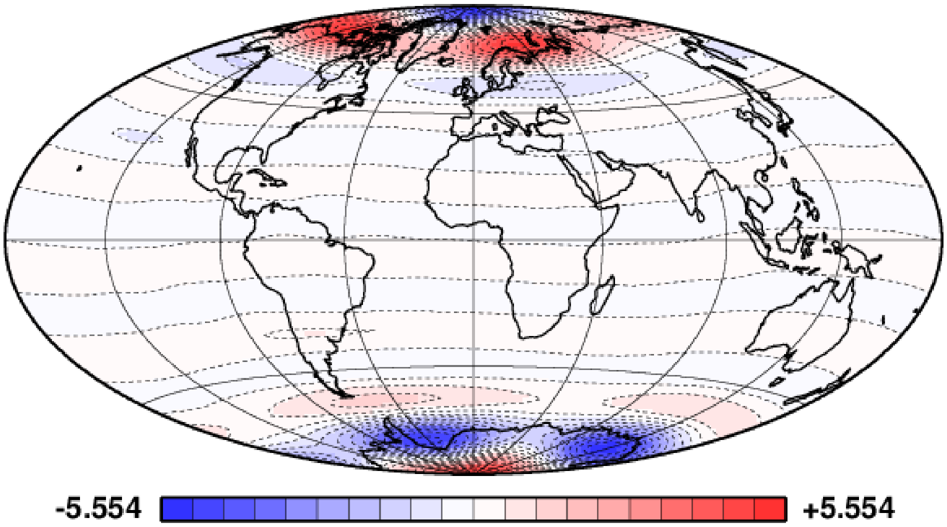

Figure 29: 2019/03/21-26 230 EEJ - Z component map, eigenvector 190, eigenvalue 21

7 Analysis

7.1 Interpreting the Chaos Residual Maps

From the maps, we can clearly see a benefit to using the EEJ, and especially the perfect equator. There are still however quite large residuals along the equator. This is clearly due to error in the determination of the EEJ points, since in the perfect equator map this effect is not nearly as pronounced. The simplest way to alleviate this effect is just with more EEJ points, we have only done the month of March 2019 in this study, perhaps 3, 6, or even 12 months is required to sufficiently average out the error over the equator. Another problem is that we have only crust-corrected a subset of points due to time limitations, therefore we only have a few points around the Bangui anomaly and any error in those will be more pronounced. The crustal field will have an effect everywhere along the equator and although not as large a magnitude of Bangui may also have a large enough effect as to increase the error in other locations along the equator.

The position of the magnetic equator, as we are measuring with the EEJ, is crucial to modelling. Any error in the equator position will be highly pronounced since the axial dipole field is highly constrained by the equator. The axial dipole is also the largest component and gives an approximate z component of

$$z = -2g_1^0 \cos\theta$$

where θ is latitude. The g_1^0 component is on the order of $30,000nT$ meaning at the equator, even a 0.1 degree error in latitude causes an error in g_1^0 around $100nT$. This explains the large Chaos residuals seen in the maps.

In the vector analysis we find that even poor quality vector data is better along the equator, although much worse at the poles. The satellite has global coverage but doesn't return data at the poles, due to the large magnetic interference of the magnetorquers which operate at polar latitudes on the satellite. However, interestingly we don't see these same problems in the intensity data.

7.2 The Eigensolution

Examining the eigenvalues and eigenvectors for our various models, it is clear the benefit of the EEJ points to the solution stability. The component of the Chaos model along the eigenvectors reveals some interesting peaks in higher degree coefficients, meaning the Chaos field has a large magnitude the direction of these eigenvectors. This is a problem as these eigenvectors (160 & 190) have very low eigenvalues, normalised to the largest eigenvalue we have 0.07 and 0.0002 respectively. These are both very low, but 21 is exceptionally low. In other words this means these eigenvectors are important to the determination of the true field (Chaos); However, the coefficients depending on these eigenvectors, following the eigenvector formulation in 4.2, are not well determined.
We can examine this further by making the familiar z component maps, but for the field from these eigenvectors. See Fig 28 and 29 for the field maps from the 160 and 190 eigenvector respectively.

From the maps, these are evidently axial dipole eigenvectors. Notice the smaller eigenvalue eigenvector has a much less well defined axial dipole signature. This is a clear illustration of the Backus effect, causing axial dipole eigenvectors with low eigenvalues, meaning the model coefficient g_1^0 is less well determined and contains a large error. Another factor in this is the lack of polar data, which also contributes to low eigenvalue dipole eigenvectors.

7.3 Conclusions & Further Research

To conclude the study, the EEJ in it's current form is not sufficient as to alleviate the Backus effect. We do see improvements in convergence and some minor improvements in the Chaos residual however, still much worse than poor-quality vector data. It is also apparent that we get convergence essentially for free with vector data, so it begs the question of why not just use vector data, even if it is bad quality.

Going back to the original aims of the study, the goal was to find a low-cost solution to field modelling. This was ultimately a failure however, we have learnt some new things about the inverse problem. The sensitivity to bad data along the equator is clearly very high, due to the problems with the dipole coefficient we have discussed.

For future work, the EEJ points will need to be revisited with a crustal field correction across the entire month. We also need to investigate the effect of more points on Chaos residual, during this study we progressively modelled with increasing numbers of points as we went and there is a positive effect on the residual. This effect tapers of around 150 points; However, with only 230 points and over half of them determined without a crust correction, it is unclear whether the limiting factor is intrinsic to the EEJ or the error in point determination.

8 Bibliography

Backus, G. E., Non-uniqueness of the external geomagnetic field determined by surface intensity measurements, J. Geophys. Res., 75, 6337– 6341, 1970

C. C. Finlay, C. Kloss, N. Olsen, M. D. Hammer, L. Tøffner-Clausen, A. Grayver & A. Kuvshinov, The CHAOS-7 geomagnetic field model and observed changes in the South Atlantic Anomaly, Earth, Planets and Space, 72, Article number: 156, 2020

GFZ German Research Centre for Geosciences, Postdam, https://kp.gfz-potsdam.de/en/
R. Holme, J. MA, H. Lühr, Magnetic field modelling from scalar-only data: Resolving the Backus effect with the equatorial electrojet, Earth planets space 57 (12), 1203-1209, 2005

R. Holme, Modelling of attitude error in vector magnetic data: application to Ørsted data, Earth Planets Space 52, 1187–1197, 2000

N. Olsen, R. Holme et al. Ørsted Initial Field Model, Geophysical Research Letters 27(22), 3607-3610, 2000

R. A. Langel, W. J. Hinze, The Magnetic Field of the Earth's Lithosphere: The Satellite Perspective, Cambridge University Press, 1998

Ultre-Guèrard P. and J. Achache, Error analysis of total field models derived from POGS data, J. Geomag. Geoelectr., 49, 453–467, 1997

S. Xuhui, Z. Xuemin, et al. State-of-the-art of the China Seismo-Electromagnetic Satellite Mission, Science China Technological Sciences, 61, 5, 634-642, 2018

Stern, D. P., R. A. Langel, and G. D. Mead, Backus effect observed by MAGSAT, Geophys. Res. Lett., 7, 941–944, 1980

World Data Center for Geomagnetism, Kyoto, https://wdc.kugi.kyoto-u.ac.jp/index.html